Differential intracavity phase spectroscopy and its application to a three-level system in samarium

Scott A. Diddams,* Jean-Claude Diels, and Briggs Atherton
Department of Physics and Astronomy, University of New Mexico, Albuquerque, New Mexico 87131
(Received 23 September 1997; revised manuscript received 23 April 1998)

A technique of differential intracavity phase spectroscopy is introduced. The measured beat frequency between the two counterpropagating fields in a ring laser directly yields the differential phase shift due to the presence of an atomic vapor. In an unstabilized laser cavity, phase differences near 10^{-6} are measured. This technique is used to study the nonlinear dispersion associated with a three-level Λ system in atomic samarium. Sub-Doppler resonances and population trapping are observed, both of which are attributed to the coherences between the two lower levels of the Λ level structure. Solutions of the density matrix describing the system are also presented, and good qualitative agreement is found between the calculations and the measurements. [S1050-2947(98)01909-X]

PACS number(s): 42.50.Md, 39.30.+w, 42.50.Gy

I. INTRODUCTION

Traditional methods of intracavity laser spectroscopy typically measure absorption—whether it be the decrease in power of a single-mode laser, hole burning in the spectrum of a broadband laser, or the fluorescence from an intracavity sample [1,2]. In contrast, the method presented here is phase sensitive, whereby changes in the index of refraction associated with a weakly absorbing transition are measured. This technique involves decoupling the two counterpropagating fields inside a ring laser and measuring the net phase difference between the fields. The phase difference, which is due to the presence of an intracavity atomic vapor, is manifest in a beat frequency $\Delta\nu$ when the counterpropagating waves are mixed together on a photodetector outside the cavity. The phase shift is therefore directly measured as a frequency, as opposed to being converted to an intensity variation (using polarization rotation, for example). Such a measurement necessarily implies that stable bidirectional operation must first be obtained, and furthermore, the two counterpropagating waves must not be frequency locked together, as is often the case in ring lasers [3,4]. In this work, the problems of frequency locking and stable bidirectional operation are overcome with a ring dye laser operating in a unique mode-locked regime [5]. Previous studies with mode-locked dye lasers have shown no measurable coupling between the counterpropagating fields. This has made possible the measurement of differential phase shifts on the order of 10^{-6}, with the unstabilized cavity being the limiting factor [6–8].

We apply this technique of differential intracavity phase spectroscopy to a three-level system in samarium vapor. The transition of interest is between a $J=1$ lower level and a $J'=0$ excited state with a resonant wavelength of 653.86 nm. The $4f^6 6s^2\ {}^7F_1$ lower state at 292.58 cm^{-1} is part of the thermally populated ground-state manifold of samarium, while the $4f^6 6s 6p\ {}^5D_0$ excited state is 15 567.32 cm^{-1} above the samarium ground state [9]. The $m_J=\pm 1$ lower levels are coupled to the $J=0$ excited state with $\sigma_\pm$-polarized fields, creating a three-level Λ system. The degeneracy of the thermally populated lower level can be removed with the application of a magnetic field. We neglect the $m_J=0$ sublevel because π-polarized light is required to couple it to the excited state. Similar transitions in samarium at wavelengths accessible to common dye lasers have been studied by several groups over the past two decades [10–16]. It is well established that Zeeman coherences between the $m_J=\pm 1$ sublevels strongly alter the real part of the polarization of the optical transition—modifying and enhancing the rotation of linear polarized light when the atomic vapor is placed between crossed polarizers [12–15,17–19]. In this work, the circular birefringence in the Λ system is studied inside the cavity of a ring dye laser. The two counterpropagating fields E_+ and E_- are given orthogonal circular polarizations, such that each field interacts with only one branch of the Λ system. Phase shifts imparted to the fields are then measured in the beat frequency between E_+ and E_-. The dependence of the beat frequency on the detuning of the fields and the separation of the $m_J=\pm 1$ lower levels is studied. Sub-Doppler resonances in the beat frequency are observed when the lower level separation matches the detunings. These resonances are attributed to the sublevel coherences which result from the interaction of the strong fields with the Λ system. Measurements of the dependence of the beat frequency on buffer gas pressure and the observation of a null in the fluorescence from the excited state confirm the presence of the sublevel coherences and population trapping. All measurements are in good qualitative agreement with the results of a steady-state theoretical calculation.

This paper is structured in the following manner. The following section contains a simple description of the principle of differential intracavity phase spectroscopy, including an order of magnitude estimate of the potential sensitivity. Section III describes the experimental setup, which employs a novel ring laser with a linear extension. As will be shown, this configuration greatly reduces the frequency stability re-

*Present address: JILA, University of Colorado, Boulder, CO 80309-0440.

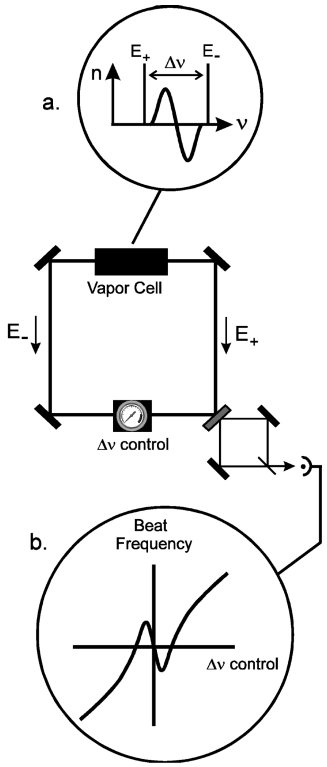

FIG. 1. (a) Differential intracavity phase spectroscopy works on the principle that different longitudinal modes in the laser can be made to interact with different parts of the dispersion curve associated with an atomic transition. (b) As the offset between the longitudinal modes is scanned the dispersionlike response is seen in the beat frequency.

strictions placed on the unstabilized laser. In Sec. IV intracavity measurements of the nonlinear birefringence in the Λ system are presented, along with observations of coherent population trapping in the Zeeman sub-levels of the Λ system. Section V outlines the simple theory behind the measurements, including steady-state solutions of the density matrix for the three-level system. And finally, in Sec. VI we conclude with a discussion of the results and suggestions of improvements and future applications.

II. PRINCIPLE OF DIFFERENTIAL INTRACAVITY PHASE SPECTROSCOPY

The principle of differential intracavity phase spectroscopy can be understood with the aid of the gedanken experiment shown in Fig. 1. To keep this illustration simple, for the moment we will use a two-level atomic system and permit only two longitudinal modes in this ring laser: one which is propagating clockwise (E_+) and the other which is propagating counterclockwise (E_-). A beat frequency between the fields is measured by interfering them on a photodiode outside the cavity as shown. With no vapor present, the beat frequency is equivalent to the frequency separation between the modes. This separation can be controlled by several means, including a nonreciprocal index difference in an electro-optic or magneto-optic crystal, or even the rotation of the laser [7,8]. For now, it is sufficient to designate the frequency control mechanism by a black box which varies the frequency separation between the modes in a linear fashion. The inset (a) of Fig. 1 provides a simple frequency domain picture of the interaction between the longitudinal modes of the ring laser (depicted as δ functions) and the index of refraction dispersion curve associated with the two-level transition. If the two modes are scanned in opposite directions across the dispersion curve, the effective cavity lengths in the two directions will be lengthened and shortened, respectively. The difference in cavity length for the two oppositely directed fields implies different resonant frequencies which results in a modulation of the beat frequency between the fields when they are mixed on a photodetector outside the cavity. In this qualitative analysis, we would expect that when the fields are near resonance the beat frequency will vary in a fashion similar to that of the index dispersion curve. The beat frequency as a function of the frequency control mechanism is shown in inset (b) of Fig. 1, where the normally linear relationship is distorted due to the presence of the resonance.

It is possible to make a simple estimate of the order of magnitude of the expected variation of the beat frequency in such an experiment. The beat frequency is the net phase difference $\Delta\phi$ per cavity round-trip time τ_{RT} such that:

$$\Delta\nu = \frac{\Delta\phi}{2\pi\tau_{\mathrm{RT}}}. \tag{1}$$

All other things in the cavity being equal, to first order $\Delta\phi$ is related to the path length difference $\Delta nL = (n_+ - n_-)L$ for the two fields propagating through the atomic vapor. Neglecting broadening mechanisms and assuming a Lorentzian line shape for the atoms, Δn is maximum when the counterpropagating fields are detuned approximately one-half linewidth on each side of line center (i.e., a detuning equal to $1/T_2$, with T_2 being the dephasing time). This means that the maximum path length difference between the counterpropagating fields is on the order of

$$(\Delta nL)_{\max} = \frac{LN|\mu|^2 T_2}{\epsilon_0 \hbar}. \tag{2}$$

In an unstabilized ring laser with a 3 m perimeter it is possible to measure differential path lengths $\Delta nL = 1$ pm [8]. If we assume a vapor of sodium atoms such that $\mu = 1.8 \times 10^{-29}$ C m, $T_2 = 32$ ns, and $L = 10$ cm, we find that this system could measure number densities below $N = 10^3$ cm^{-3}. The corresponding linear absorption coefficient for a vapor of this density would be on the order of $\alpha = 10^{-6}$ cm^{-1}. With active stabilization of the laser cavity, it is not unreasonable to expect an improvement in sensitivity of 3–5 orders of magnitude. Following the above example, this would permit measurements on very weak transitions (or very few atoms) with α approaching 10^{-11} cm^{-1}. Such sensitivity could be comparable to that of established techniques [1,2,20,21]. As will be discussed in further detail, the same laser can be equally sensitive to circular birefringence. The current sensitivity in $\Delta\phi$ of 10^{-6} is only an order of magnitude less than that which can be attained with the best polarizers. Here again, active stabilization of the laser cavity could improve this sensitivity to 10^{-9} or better. At this level, the ring laser would be an unparalled detector of birefrin-

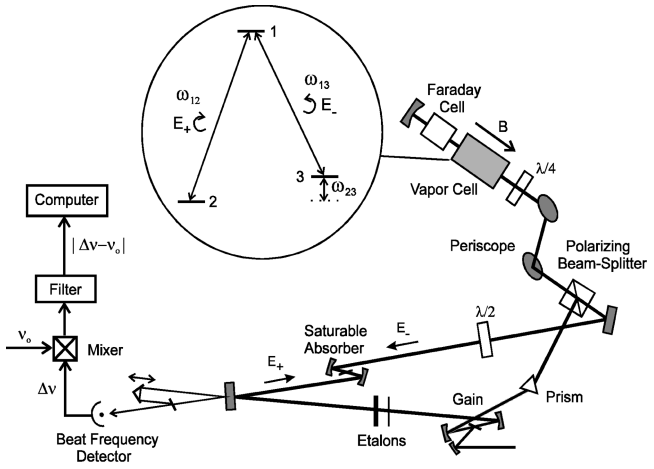

FIG. 2. Ring laser with a linear extension (tail) used for intracavity spectroscopy experiments of a three-level atomic system. See text for details.

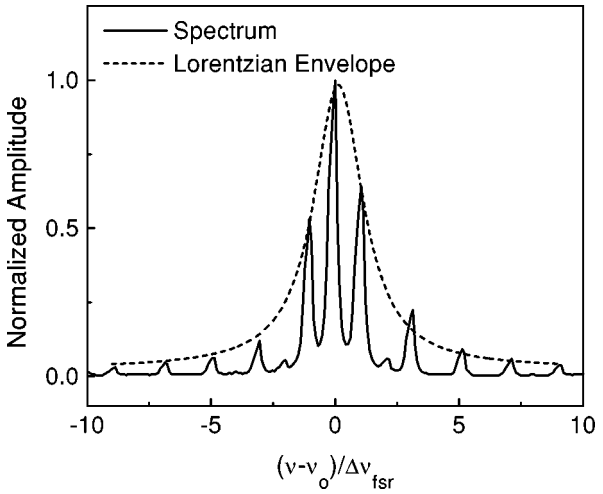

FIG. 3. Spectrum of the laser of Fig. 2 as measured with a scanning Fabry-Pérot interferometer. The solid line is the data and the dashed line is a Lorentzian fit to the envelope. The width of the individual modes is given by the instrument resolution. The presence of only the odd harmonics is expected from the square-wave output of the laser. The frequency axis is normalized by the free spectral range of the laser cavity, which is approximately $\Delta\nu_{\mathrm{FSR}} = 75$ MHz.

gence, making it a potential tool for experimental measurements of parity non-conserving optical rotation [22–24].

III. EXPERIMENTAL SETUP

The experimental apparatus employed for differential intracavity phase spectroscopy is shown in Fig. 2. The laser is a modified version of a femtosecond mode-locked ring dye laser used in previous measurements of nonreciprocal phase differences [8]. The gain medium is DCM (dicyanmethylene) in a 2–3 mMolar solution with equal parts ethylene glycol and EPH (Exciton trade name), and the saturable absorber is a weak solution ($\sim$0.05 mMolar) of DQTCI (diethylquinolylthiacarbocyanine iodide) in equal parts of ethanol and EPH. The gain is pumped with 4–8 W of the multiline output of an argon ion laser, which is about 2–3 times the cw threshold. The flowing gain and saturable absorber jets are separated by approximately 1/4 of the cavity perimeter. There are three modifications in particular which make this laser different from the more familiar femtosecond ring dye laser: (1) the addition of the linear part of the cavity, which has been named the ''tail,'' (2) the use of two étalons to limit the cavity bandwidth, and (3) the operation of the laser with a weak saturable absorber. The immediate result of the étalons and the weak saturable absorber is that femtosecond pulses are no longer obtained. The more surprising result is that the output of the laser now consists of two counterpropagating trains of square pulses with period equal to the cavity round-trip time ($\tau_{\mathrm{RT}} = P/c$, where P is the perimeter and c is the speed of light) [5]. The spectrum of one of the outputs of the laser operating in this mode was measured with a scanning Fabry-Pérot interferometer, and the result is shown in Fig. 3. The spectrum is plotted as a function of the frequency normalized by the free spectral range (FSR) of the laser cavity, which is approximately 75 MHz. (With respect to the units of frequency, in this work we always use units of Hz to refer to cyclic frequencies, while units of s^{-1} refer to angular frequencies.) As shown, the laser is multimode with its output consisting of a fundamental frequency plus odd harmonics at both higher and lower frequencies. This is the expected Fourier composition for a train of square pulses. From Fig. 3 we determine that the bandwidth of the laser is on the order of 150 MHz, with the majority of the power contained in just three modes. We note that multimode operation is not necessarily the preferred one. Indeed, it would be optimal to have the ring laser operating with just two counterpropagating modes. However, two-mode ring lasers with homogeneously broadened gain generally exhibit random switching between the counterpropagating modes [25]. In contrast, the multimode operation of the laser in Fig. 2 has proven to have good stability such that a clean beat frequency is generated when the counterpropagating fields are mixed on a photodiode as shown in the figure.

The addition of the 85 cm tail to the ring laser is accomplished with a quarter-wave plate ($\lambda/4$), a half-wave plate ($\lambda/2$), and a polarizing beam splitter. The wave plates are zero order and antireflection coated, while the polarizing beam splitter consists of two cemented calcite trapezoids (antireflection coated on their faces). The extinction ratio of the polarizing beam splitter was measured to be better than 10^{-5}, and the insertion losses were on the order of 1%. The presence of the $\lambda/4$ plate gives the two counterpropagating waves opposite circular polarizations (with respect to the axis determined by the magnetic field) once they enter the tail. The second pass through the $\lambda/4$ plate then converts the circularly polarized light back to the appropriate linear polarization so that it continues around the ring in the same direction it was traveling before entering the tail. The angle of incidence on the curved mirror at the end of the tail deviates from the normal by a few milliradians, such that any small leakage through the polarizing beam splitter is not injected into the counterpropagating wave. The linear tail contains a stainless steel vapor cell where samarium metal is heated to temperatures between 550 and 750 °C. Partial pressures of samarium for these temperatures range from 0.043 to 17 mTorr [26]. The heated region of the cell is 5 cm in length, such that the total interaction length is $d = 10$ cm.

Heating is provided by helically wound dc electrical coils, and neon buffer gas is added at a minimum partial pressure of 10 mTorr to provide sufficient collisions to keep the windows of the cell clean. Three orthogonal sets of Helmholtz coils surround the cell, providing a means of nulling constant external magnetic fields and providing a variable field along the direction of light propagation. An additional detail regarding the tail is that it contains a periscope to raise the beam to 30 cm above the optical table during its traversal of the vapor cell. This was done so that Helmholtz coils of the largest practical diameter could be used.The linear tail is also a convenient means of providing a frequency offset between the counterpropagating modes. This is accomplished with a Faraday cell comprised of a permanent magnet and a 13 mm long piece of anti-reflection coated BK-7 glass. Because the BK-7 exhibits circular birefringence the two orthogonally polarized fields experience a differential shift in cavity length which results in an offset (or bias) $\Delta\nu_b$ between the longitudinal modes of the two fields. This bias is directly measured in the beat frequency. By translating the BK-7 through the permanent magnetic field, $\Delta\nu_b$ can be varied continuously over ± 2 MHz.

The primary reason for using the linear extension of the ring cavity is that it relaxes the requirements on the frequency stability of the laser. This is because the two *counterpropagating* waves from the ring laser now *copropagate* through the tail—thereby interacting with the same Doppler velocity group of atoms. This is in contrast to the case where two waves counterpropagate through a vapor and only interact with the same velocity group of atoms if they are tuned exactly to line center. In the tail of Fig. 2 there can be an interaction between two counterpropagating waves in the vapor; however, the probability of the two counterpropagating waves being tuned to exactly line center is small (on the order of the ratio of the linewidth of a laser mode to the width of the Doppler broadened line). Therefore standing wave interference effects are negligible and the interaction between the laser and the samarium can be treated as two fields copropagating through a vapor having effectively double the length. We do, however, briefly consider the interaction of counterpropagating fields in the Appendix.

The frequency control of the laser is coarse, consisting of just the single prism and two étalons. By adjusting the angle of the beam on the prism, the laser can be tuned by hand over many tens of nanometers. One of the étalons is a 100 μm thick piece of uncoated fused silica while the second étalon is 500 μm thick and coated to have a reflectivity of about 30%. With the combination of the prism and the two étalons, it is possible to tune the laser to resonance with the 653.86 nm transition between the $4f^6 6s^2\ {}^7F_1$ lower level and the $4f^6 6s6p\ {}^5D_0$ excited state. In tuning to resonance, fluorescence is observed by eye and the wavelength of the laser is measured with a monochromator. Care was taken to avoid three other nearby transitions, all within ± 1 nm of the 653.86 nm transition. Since no active stabilization of the laser cavity is employed, mirror vibrations and table resonances account for a constant motion (at mechanical resonance frequencies in the 1–100 Hz range) of the comb of modes about the transition frequency. Despite this ''tremor'' of the modes, approximate resonance is maintained typically for 30–60 minutes. This is a sufficient time to perform several sets of measurements.

Naturally occurring samarium, as was used in this work, consists of seven isotopes. The five even isotopes are 71% abundant and have no nuclear spin. The two odd isotopes, with nuclear spin equal to $I=7/2$, comprise the remaining 29% of the sample. The shift of the transition resonance frequency for the various isotopes has been measured using standard saturation spectroscopy [27]. Similar to measurements on other samarium transitions [11,28], the resonant frequencies of the isotopes are spread over about 8 GHz, with the two most abundant isotopes (^{154}Sm and ^{152}Sm) being well separated from the odd isotopes by 3 GHz. Previous studies have taken advantage of this relatively large separation to isolate only ^{154}Sm and ^{152}Sm. However, since the laser of Fig. 2 is not single mode and employs only coarse tuning, it was impossible to determine with which isotope(s) the laser was tuned to resonance for a particular measurement. Of particular concern are the two odd isotopes because their ground states have a $2F+1$ degeneracy with $F=I+J=9/2$, 7/2, or 5/2. Here, the application of a magnetic field no longer results in the desired three-level system. Interestingly, it has been observed that for low buffer gas pressures, the contribution to Faraday rotation from the odd isotopes is small or nonexistent [12,14,15,27]. This is believed to be due to optical pumping between the multitude of hyperfine levels. In the simple three-level system with two driving fields Zeeman coherences develop as the population is transferred back and forth between the $m_J=\pm 1$ sublevels. This is in contrast to the situation of the odd isotopes where optical pumping will tend to isolate population in some of the $2F+1$ sublevels, thereby preventing the formation of Zeeman coherences. For these reasons, we will assume the contribution of the odd samarium isotopes to the following measurements to be small.

IV. MEASUREMENTS

With the laser tuned to the $J=1\rightarrow J'=0$ transition, the two orthogonally polarized fields from the ring individually interact with only one branch of the Λ transition in samarium. This is illustrated in the inset of Fig. 2. When the splitting between the lower levels equals $\Delta\nu_b$, the fields E_+ and E_- are both in resonance with transitions $2\rightarrow 1$ and $3\rightarrow 1$. Any resonant changes in the index of refraction of the samarium are manifest in the beat frequency in a manner similar to what was initially described by Fig. 1. The beat frequency is measured by taking the outputs of the laser from the two directions and mixing them on a standard photodiode. A simple delay line, as shown in Fig. 2, is used to provide optimal temporal overlap of the two square pulse fields at the photodiode. The output of the photodiode is mixed with a reference oscillator at frequency ν_0, producing a difference frequency $|\Delta\nu-\nu_0|$ which can be sampled with an inexpensive analog-to-digital (AD) card. With the laser tuned to resonance with the transition, a triangle-wave voltage is applied to the axial Helmholtz coils. This voltage and the difference frequency $|\Delta\nu-\nu_0|$ are simultaneously digitized and stored on a computer. The raw data from such a measurement are shown in Fig. 4(a). In these data, the bias beat frequency applied with the Faraday cell was $\Delta\nu_b$

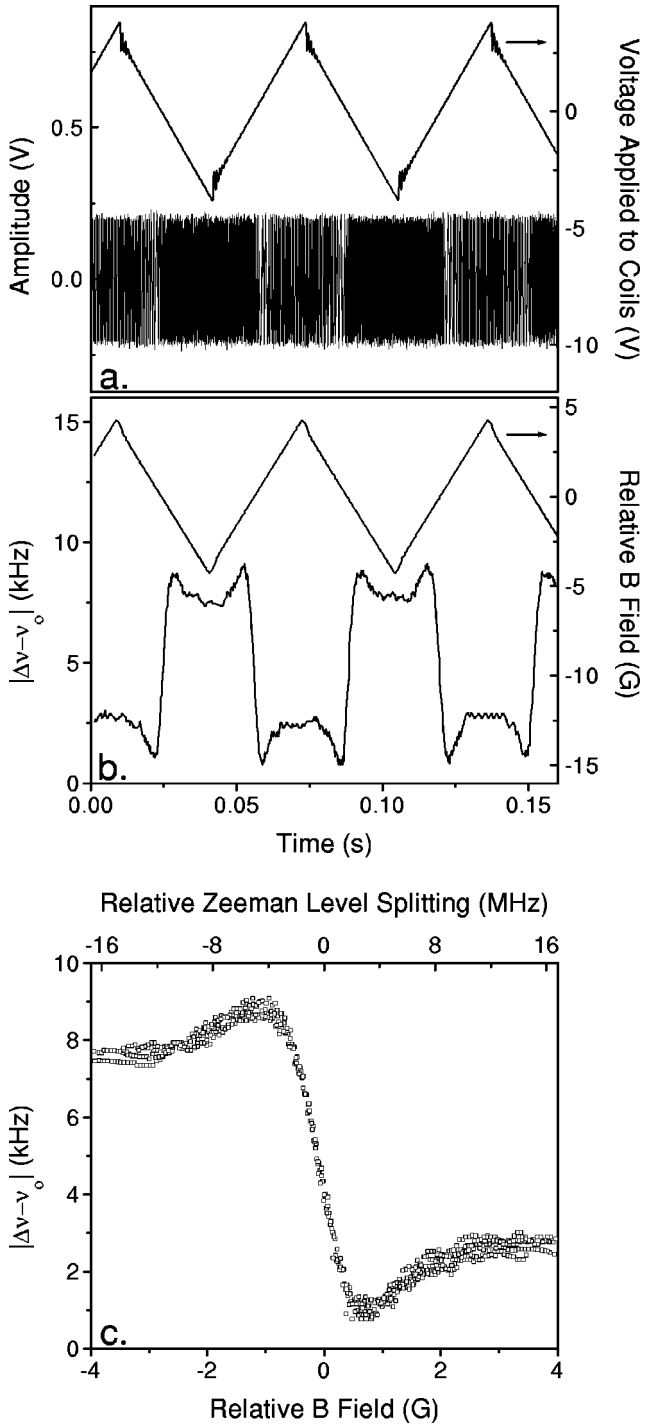

FIG. 4. (a) Digitally sampled beat frequency and voltage applied to the axial Helmholtz coils. The small ringing near the top of the triangle wave is an artifact of the wave form generator. (b) and (c) The same data as above after calibration of the magnetic field and beat frequency. In (c) the beat frequency is plotted versus the magnetic field. The zero of the magnetic field has an error of ± 1 G for this data.

$=1.105$ MHz, and the reference oscillator frequency was $\nu_0=1.0950$ MHz. Neon buffer gas was added to a partial pressure of 20 mTorr, and the temperature of the vapor cell was 530 °C. At this temperature, the partial pressure of samarium is 5×10^{-6} Torr, and the number density is $\sim 5\times10^{10}$ cm^{-3} for ^{152}Sm. Using the measured dipole moment of $|\mu|=7.5\times10^{-31}$ C m [27], this implies an optical density of $\alpha L=0.005$ at the center of the Doppler-broadened line. The beat frequency at each value of the magnetic field is determined by performing a Fourier transform in a moving time window of typically 128 or 256 data points. The centroid of the frequency spectrum is computed and designated as the average frequency in each time window. The result is shown in Fig. 4(b), where the resonant type behavior of the beat frequency is now clear. This is even more obvious if the beat frequency is plotted as a function of the magnetic field as is done in Fig. 4(c). In this plot, the accumulated (unaveraged) data from four complete scans of the magnetic field are shown. The resolution of the beat frequency measurement is on the order of 100 Hz. From Eq. (1), this implies an uncertainty in the measured differential phase shift of 8×10^{-6} if $\tau_{RT}=13.4$ ns.

The dispersionlike resonance of Fig. 4(c), with a sharp change in the beat frequency occurring over a few Gauss, is characteristic of all measurements which we present. The resonance is quite narrow, in view of the large Doppler width of the the transition, and the absence of mode stabilization discussed earlier. The $J=1$ lower level has a Landé factor $g_J=1.5$ from which we calculate the lower level splitting to be $\omega_{23}=(2\pi)4.2\times10^6$ s^{-1}/G. This relationship is used to define the upper axis of Fig. 4(c). As can be seen, the observed resonance is on the order of 5 MHz wide. This is much less than the Doppler-broadened linewidth ($\sim$800 MHz full width at half maximum) and provides convincing evidence of the Doppler-free nature of the measurement. The narrowness of the resonance is due to the two strong fields transferring population between the Zeeman sublevels and the resulting coherences which are established between these sublevels. The dispersionlike shape of the resonance observed in the beat frequency is similar to the nonlinear Faraday rotation measured with samarium vapor placed between crossed polarizers [13,14]. Indeed, what is being measured in the ring laser is the phase difference between the right and left circularly polarized fields as they interact with the samarium vapor. Whereas the more traditional intensity measurements result in symmetric signals, the direct phase measurements presented here are asymmetric. With regard to this difference, there is always an ambiguity in the sign of the measurements made with the ring laser unless it is known which of the two counterpropagating waves receives the larger (or smaller) phase shift. However, this difficulty could be resolved with a dual-element detector, as is used in laser gyroscopes. Furthermore, the particular choice of the reference oscillator frequency ν_0 is also arbitrary. If for the data of Fig. 4 we had chosen ν_0 to be smaller than the bias beat frequency, the maximum of $|\Delta\nu-\nu_0|$ would occur on the right side of the figure rather than the left. This ambiguity will be seen in subsequent data.

If the dispersionlike shape of the beat frequency is the result of coherent interactions when both fields are tuned to resonance, one would expect the resonance to be centered at the value of the lower level splitting, ω_{23}, which is equal to the bias beat frequency $\Delta\nu_b$. The data of Fig. 5 are such an example. Here two sets of data were taken for two different orientations of the permanent magnet of the Faraday cell. With the magnet in one orientation, a bias beat frequency was set at $\Delta\nu_b=2$ MHz, and the reference oscillator fre-

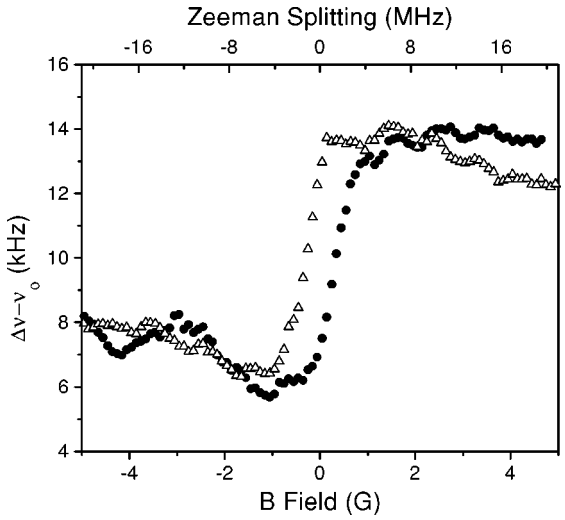

FIG. 5. Two sets of data taken with two different beat frequency biases. For the triangles $\Delta\nu_b=-2$ MHz, while for the circles $\Delta\nu_b=+2$ MHz.

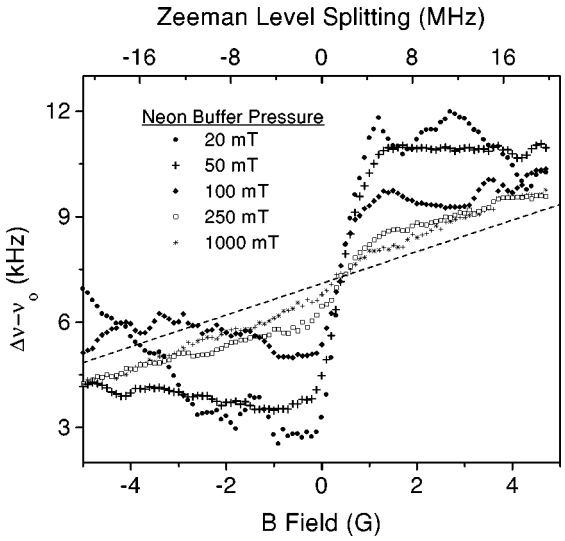

FIG. 6. Dependence of the beat frequency on the neon buffer gas pressure. The five sets of data points are for the five different buffer gas pressures as indicated. The dashed line is the linear response of the beat frequency due to the vapor cell windows.

quency was close to this. This resulted in the circular data points in the figure. The orientation of the magnet was then reversed so that the sign of the bias beat frequency is reversed to $\Delta\nu_b=-2$ MHz. This resulted in the triangle data points of Fig. 5. In both cases, the data points are beat frequency values averaged over several scans of the magnetic field. The two curves are shifted equally in opposite directions from the zero magnetic field point, although the shift is closer to ± 1.5 MHz than the expected ± 2 MHz. Repeated measurements always resulted in a shift less than what is expected, indicating a systematic error in the calibration or alignment of the magnetic fields.

One might consider mode pulling by the resonant atomic vapor to be an explanation for the discrepancy in the positions of the resonance of Fig. 5. In a dispersionless cold cavity, the longitudinal modes are equally spaced such that the round-trip phase shift experienced by a mode at frequency ω is $\omega P/c$. However, the addition of a resonant atomic medium provides an additional phase shift given by $\omega n_\omega d/c$, where d is the total interaction length of the medium and, n_ω is its index at frequency ω. This extra phase shift means that the cold-cavity mode must shift in frequency such that the total round-trip phase shift is still an integer number of 2π. To first order, the shift in frequency is given by $\delta\omega=\omega n_\omega d/(c\tau_{\mathrm{RT}})$ [29]. This, however, is simply the beat frequency. For the data of Fig. 5, this means that the mode pulling would only be on the order of a few kilohertz which is too small to explain the 1 MHz discrepancy in this figure.

The dependence of the beat frequency on the buffer gas pressure was also explored. The results are presented in Fig. 6. For the data of this figure, the temperature of the vapor cell was held constant at 538 °C. The laser was tuned to resonance with the 653.86 nm transition, and data were acquired as described above. A bias of $\Delta\nu_b=1.95$ MHz was applied, and the frequency of the reference oscillator was adjusted to be slightly lower than the bias. The pressure of the neon buffer gas was then varied and five sets of beat frequency data were recorded. After calibration and averaging over several scans of the magnetic field, the data sets shown in Fig. 6 were obtained. For display purposes each curve was slightly shifted up or down so that the point of symmetry along the y axis for each curve was the same. This is equivalent to having made small adjustments in ν_0 for each curve. In addition, the center of the resonance for all curves lies close to a level splitting of about 2 MHz, which is the expected value for the applied bias. At the lower buffer gas pressures, a very sharp jump in the beat frequency is observed, similar to what was presented in Fig. 4. As the neon pressure is increased, the resonance starts to disappear and the magnetic field dependence approaches the linear response which is due to the two windows on the vapor cell (dashed line in the figure). The decrease in the amplitude of the resonance with increasing buffer gas pressure is to be expected if the resonance is indeed due to Zeeman coherences. This is because dephasing collisions which destroy the coherences also increase with the increasing neon pressure.

The simultaneous measurement of the resonant fluorescence with the setup of Fig. 2 further illustrates the presence of the Zeeman coherences in the interaction of the fields with the samarium. This was done by imaging the fluorescence into a large diameter optical fiber with a microscope objective. The output of the fiber was sent into a 0.24 m monochromator, which was set to pass light at 653.86 nm, with a 1 nm bandwidth. The throughput of the monochromator was detected with a photomultiplier tube (PMT). With the oven heated to 550 °C, and 40 mTorr of neon buffer gas in the cell, the magnetic field was scanned and the beat frequency and fluorescence were recorded. No bias beat frequency was applied and no reference oscillator was used, so that the true beat frequency was sampled. The calibrated results are shown in Fig. 7. In this figure the applied magnetic field is shown in arbitrary units in the upper plot, while the calibrated beat frequency and PMT signals are shown in the lower plot. Because a PMT was used, a more negative signal implies higher fluorescence intensity. With no applied bias, the interaction with the samarium was sufficient to drive the beat frequency through zero. As there is no way to distin-

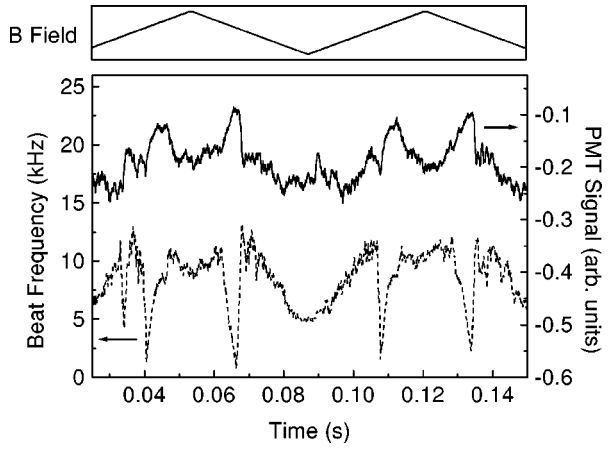

FIG. 7. Calibrated beat frequency (dashed line) and excited-state fluorescence (solid line) of as a function of time. As the fluorescence was detected with a photomultiplier, lower light levels result in less negative signals. The time varying applied magnetic field (arbitrary units) is shown in the small upper plot. The time axes of both plots are the same.

guish between positive and negative beat frequencies in this measurement, the beat frequency has v-shaped structures in contrast to the structure of the signals in Figs. 4–6. The interesting feature of this data is the correlation that exists between the beat frequency and the fluorescence. It is seen that near the resonance in the beat frequency (zero magnetic field), the fluorescence intensity decreases by about 50%. A similar decrease in fluorescence, or the dark state, was observed and studied about 20 years ago with three-level systems found in the hyperfine structure of sodium [30–33]. The interpretation of the present results is the same as what was presented in these past works. The fluorescence signal drops when both fields come into resonance with the same Doppler velocity group because the atoms are optically pumped and trapped in a coherent superposition of the $m_J = \pm 1$ sublevels. The atoms in this coherent state are no longer able to absorb the two fields because destructive interference occurs between the excitation amplitudes on the two transitions [33]. Closer inspection of Fig. 7 shows that an asymmetry exists between the signal associated with the two different slopes of the applied magnetic field. Indeed, the drop in fluorescence associated with the rising magnetic field is delayed with respect to the beat frequency resonance. This behavior is currently not understood. It is also worth mentioning that the average intensities of the counterpropagating waves were also monitored in this experiment, but no changes correlated to the decrease in fluorescence were observed. This is indicative of the sensitivity of the phase (as opposed to amplitude) measurement, and the fact that the decrease in fluorescence is proportionately greater than any detectable change in the laser intensity.

V. THEORY

The presence of sub-Doppler resonances and population trapping, as evidenced by the data of the preceding section, calls for a nonlinear theory. If only linear dispersion is considered, the beat frequency should be representative of the different indices of refraction experienced by the two counterpropagating fields as they interact with the two different Doppler-broadened transitions of the Λ system in samarium. The characteristic width of the structure on the beat frequency in this case would be determined by the Doppler-broadened profile, which has a full width half maximum (FWHM) value greater than 800 MHz. This is about two orders of magnitude greater than the characteristic width of the measured resonance in Fig. 4(c). In order to account for the narrow resonances, a simple nonlinear theory based on the density matrix formalism will be used to handle this problem [17,12,13].

To calculate the beat frequency, one must determine the differential phase shift experienced by the fields E_+ and E_- passing through the vapor cell. This will be done by calculating the Doppler-averaged complex susceptibilities χ_+ and χ_- for each leg of the Λ transition. As already noted, the inclusion of the tail in the ring laser simplifies this analysis, allowing us to reduce the problem to one of calculating the differential phase shift between the fields as they copropagate through the vapor cell. Initially we assume that E_+ and E_- each consist of a single longitudinal mode, and we solve the density matrix equations in steady state. This assumption is a valid starting point because the spectrum of the laser (Fig. 3) consists of only a few strong longitudinal modes. The approximation of single longitudinal modes neglects that the measured beat frequency is the average of the beat frequencies between the all counterpropagating pairs of longitudinal modes which comprise E_+ and E_-. Later, the steady-state contribution of several modes will be considered. As will be seen, these results are similar to the single longitudinal mode results.

With reference to the circular inset of Fig. 2, we define the time dependence for the two counterpropagating fields by $E_+ = (\mathcal{E}_+ e^{i\omega_+ t} + \text{c.c.})/2$, and $E_- = (\mathcal{E}_- e^{i\omega_- t} + \text{c.c.})/2$, where $\mathcal{E}_+$ and $\mathcal{E}_-$ are generally time-dependent, complex amplitudes. We further assume that E_+ has right circular polarization such that it only couples the $m_J = +1$ lower level (2) to the upper level, while E_- has left circular polarization such that it only couples the $m_J = -1$ sublevel (3) to the upper level. Nine coupled differential equations describe the time evolution of the level populations and coherences within the rotating wave and slowly varying amplitude approximations:

$$\dot{\rho}_{11} = -i[\kappa\mathcal{E}_+\sigma_{21}^* - \kappa\mathcal{E}_+^*\sigma_{21} + \kappa\mathcal{E}_-\sigma_{31}^* - \kappa\mathcal{E}_-^*\sigma_{31} +] - \Gamma_1\rho_{11},$$

$$\dot{\rho}_{22} = i[\kappa\mathcal{E}_+\sigma_{21}^* - \kappa\mathcal{E}_+^*\sigma_{21}] + \frac{\Gamma_1}{2}\rho_{11} + \gamma(\rho_{33} - \rho_{22}),$$

$$\dot{\rho}_{33} = i[\kappa\mathcal{E}_-\sigma_{31}^* - \kappa\mathcal{E}_-^*\sigma_{31}] + \frac{\Gamma_1}{2}\rho_{11} + \gamma(\rho_{22} - \rho_{33}), \quad (3)$$

$$\dot{\sigma}_{21} = \dot{\sigma}_{12}^* = -i(\Delta_+ - i\gamma_{12})\sigma_{21} + i\kappa\mathcal{E}_+(\rho_{11} - \rho_{22}) - i\kappa\mathcal{E}_-\sigma_{23},$$

$$\dot{\sigma}_{31} = \dot{\sigma}_{13}^* = -i(\Delta_- - i\gamma_{13})\sigma_{31} + i\kappa\mathcal{E}_-(\rho_{11} - \rho_{33}) - i\kappa\mathcal{E}_+\sigma_{23}^*,$$

$$\dot{\sigma}_{23} = \dot{\sigma}_{32}^* = -i(\Delta_+ - \Delta_- - i\gamma_{23})\sigma_{23} + i\kappa\mathcal{E}_+\sigma_{31}^* - i\kappa\mathcal{E}_-^*\sigma_{21}.$$

In Eqs. (3), σ_{ij} are slowly varying amplitudes of the off-diagonal density matrix elements, such that $\rho_{21} = \sigma_{21}\exp(i\omega_+ t)$, $\rho_{31} = \sigma_{31}\exp(i\omega_- t)$, and $\rho_{23} = \sigma_{23}\exp[i(\omega_+$

TABLE I. Values of various rates and parameters. The neon buffer gas pressure (P_{ne}) was taken to be 10 mTorr. These values were used in all calculations, unless specifically noted in the text.

Quantity	Symbol	10^6 s^{-1}
Excited state relaxation rate	Γ_1	$(2\pi)0.17$
Natural linewidth	γ_{nat}	$(2\pi)0.085$
Transit time broadening rate	γ_{trans}	$(2\pi)0.1$
Collision rate	γ, γ_{col}	$(2\pi)0.0025\times P_{ne}$(mTorr)
Polarization relaxation rate	γ_{12}, γ_{13}	$\gamma_{trans}+\gamma_{nat}+\gamma_{col}$
Coherence relaxation rate	γ_{23}	$\gamma_{trans}+(2\pi)0.0003\times P_{ne}$(mTorr)
Doppler width (FWHM)	ω_D	$(2\pi)830.0$
Rabi frequencies	$\kappa\mathcal{E}_+, \kappa\mathcal{E}_-$	$(2\pi)2.0$

$-\omega_-)t]$. The detunings of the fields are given by $\Delta_+=\omega_+ -\omega_{12}$ and $\Delta_-=\omega_- -\omega_{13}$, where $\omega_{12}=\omega_1-\omega_2$, and $\omega_{13}=\omega_1-\omega_3$. In addition, we have let $\kappa=\mu/(2\hbar)$, with μ being the dipole moment of both optical transitions. Using this notation, in what follows we will refer to the Rabi frequencies on the two transitions as $\kappa\mathcal{E}_\pm$. We note that we have also considered the interaction of two counterpropagating linearly polarized fields tuned to the line center of the Doppler-broadened transition. A sample numerical result of this situation is shown in the Appendix.

In the above analysis, we have omitted the $m_J=0$ lower level because it is not directly coupled to the excited state by the optical fields. In a closed system this raises the issue of population trapping in $m_J=0$. However, both collisions and the rate at which atoms move through the interaction region minimize trapping in $m_J=0$ by incoherently transferring population to the $m_J=\pm1$ levels. Furthermore, in this situation, the rate of population decay from the excited state is much less than the Rabi frequencies of the optically coupled transitions—making the decay terms less important in the evolution of the density matrix elements. To a good approximation the $m_J=0$ level can be seen as an intermediate level for incoherent population transfer between the excited state and $m_J=\pm1$, and can therefore be neglected. We have phenomenologically included incoherent population transfer between the ground states in the density matrix equations with terms proportional to γ. We further note that the simplified system considered here gives results constant with descriptions of the complete four-level system [13].

The other relaxation terms included in Eqs. (3) are defined as follows. Spontaneous emission from the excited state occurs at a rate Γ_1. The relaxation rates of the polarizations are given by $\gamma_{12}=\gamma_{13}=\gamma_{nat}+\gamma_{col}$, where the natural linewidth is $\gamma_{nat}=(2\pi)85\times10^3$ s^{-1} [27]. Measurements of γ_{col} have not been reported for this transition. As an estimate, we will use a value of $\gamma_{col}=(2\pi)2.5\times10^3$ s^{-1} per mTorr, which was given by Parigger *et al.* for argon buffer gas and the $J=1\rightarrow J'=0$ samarium transition at 571 nm at 727 °C [11]. The relaxation rate of the ground-state coherence is also largely determined by the collision rate. However, as observed in several studies, for the same buffer gas pressure this rate can be significantly lower than γ_{col} [11,34,16]. McLean *et al.* have measured the orientational relaxation rate for coherences in the $J=1$ ground state and report a cross section of about 5 Å^2, for depolarizing collisions with neon buffer gas [16]. From this cross section we calculate the relaxation rate to be $\gamma_{23}=(2\pi)300$ s^{-1} per mTorr of neon at 500 °C. As can be seen, this is about an order of magnitude less than the collisional dephasing rate for the optical transition. Finally, it is important to note that the free flight of the samarium atoms through the laser beam (diameter ~3 mm) leads to transit time broadening on the order of $(2\pi)100\times10^3$ s^{-1}. This broadening affects both the natural linewidth and the lower level decoherence rate, so that in the absence of buffer gas $\gamma_{12}=\gamma_{13}=(2\pi)185\times10^3$ s^{-1} and $\gamma_{23}=(2\pi)100\times10^3$ s^{-1}. The relaxation rates used in subsequent calculations, as well as other parameters important to these calculations, are summarized in Table I.

Steady-state solutions to Eqs. (3) are obtained by setting the time derivatives equal to zero. In this case, Eqs. (3) reduces to a set of linear equations which are solved with numerical techniques. The contributions of the various Doppler velocity groups in the hot vapor cell are numerically integrated, and the resulting values of the Doppler-integrated density matrix elements $\overline{\sigma_{ij}}$ are used to obtain the susceptibility for the counterpropagating fields:

$$\chi_+=\frac{N\mu^2}{\hbar\epsilon_0\kappa\mathcal{E}_+}\{\overline{\sigma}_{12}^{(r)}-i\overline{\sigma}_{12}^{(i)}\},$$
$$\chi_-=\frac{N\mu^2}{\hbar\epsilon_0\kappa\mathcal{E}_-}\{\overline{\sigma}_{13}^{(r)}-i\overline{\sigma}_{13}^{(i)}\}. \tag{4}$$

In these equations, the superscripts (r) and (i) refer to the real and imaginary part of the complex-valued $\overline{\sigma_{ij}}$. The phase shifts experienced by the fields E_+ and E_- each round-trip due to the interaction with the samarium are proportional to the real part of the susceptibility. The net phase difference per round-trip is the expected beat frequency $\Delta\nu$, which can be written in the following form:

$$\Delta\nu=\frac{d}{\lambda\tau_{RT}}\frac{N\mu^2}{2\hbar\epsilon_0}\left\{\frac{\overline{\sigma}_{12}^{(r)}}{\kappa\mathcal{E}_+}-\frac{\overline{\sigma}_{13}^{(r)}}{\kappa\mathcal{E}_-}\right\}, \tag{5}$$

where d is the total interaction path length, λ is the average wavelength and τ_{RT} is the cavity round-trip time. In all following results, Eq. (5) has been evaluated using the values of $d=10$ cm, $\tau_{RT}=13.3$ ns, $\lambda=654$ nm, $\mu=7.5\times10^{-31}$ C m, and $N=5\times10^{10}$ cm^{-3} (the latter corresponds to a vapor at $T=525$ °C). The results of the calculations can now be used to compare the measured and calculated values of the beat

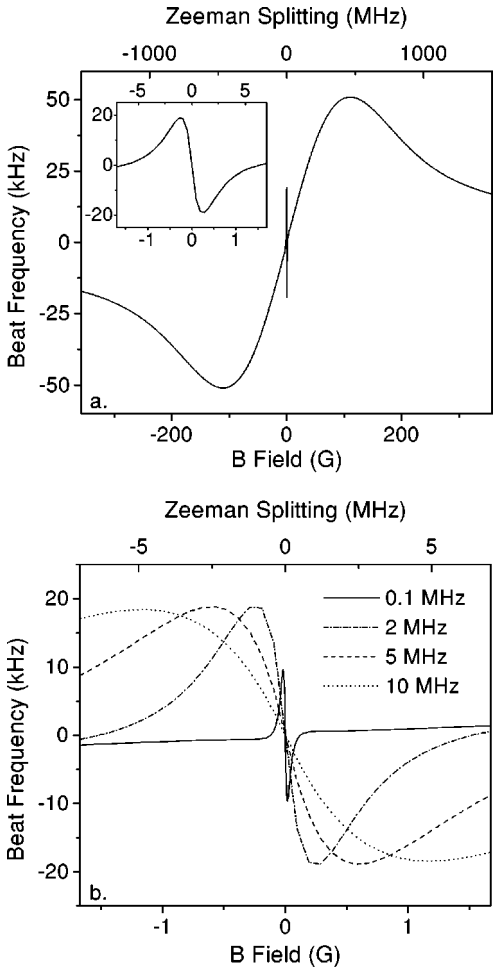

FIG. 8. Calculation of the dependence of the beat frequency on magnetic field. The sharp features in the center of the smooth curve in (a) are characteristic of the nonlinear Faraday effect. The inset of (a) shows these features in greater detail. Just the sharp features about zero magnetic field are shown in (b), where the beat frequency as a function of the magnetic field is plotted for different values of the Rabi frequencies. The given Rabi frequencies are the same for both fields.

frequency. We point out that the following numerical results are not intended to be theoretical fits to the measured data, because the experimental parameters–in particular the detuning with respect to the optical transition–cannot be sufficiently controlled to make meaningful quantitative comparisons. Instead, the results of this section are presented in order to make qualitative comparisons and confirm the physics underlying the most important features of the data. In general these qualitative comparisons are found to be in good agreement with the measured data.

The results shown in Fig. 8(a) demonstrate the transition from the linear to the nonlinear regime. Except for the sharp central feature in the middle of the graph, the overall shape of the graph of Fig. 8(a) is identical to that obtained from linear theory. This particular narrow feature is shown expanded in the inset of Fig. 8(a). This rapid change in the beat frequency near zero magnetic field is the result of the strong fields coming into resonance with the same Doppler velocity group of atoms and coherently transferring population between the two sublevels via the excited state. It is worth emphasizing that it is the strength of the fields which create the narrow resonance and distinguish it from the linear Faraday effect. For Fig. 8(a), both fields were assumed to be tuned to Doppler line center at zero magnetic field. When the intensity of the optical radiation $I=c\epsilon_0|\mathcal{E}|^2/2$ is expressed in terms of the Rabi frequency, one finds:

$$I=\frac{2\epsilon_0 c\hbar^2(\kappa\mathcal{E})^2}{\mu^2}. \tag{6}$$

For $\kappa\mathcal{E}=(2\pi)2\times10^6\ \mathrm{s}^{-1}$, the intensity is $I=1.6\ \mathrm{W/cm}^2$, which is much greater than the saturation intensity of the transition.

The dependence of the nonlinear Faraday effect on the intensity of the two fields was explored further, and the results are shown in Fig. 8(b). For these data, the Rabi frequencies of the fields (assumed equal) were varied between $(2\pi)0.1\times10^6\ \mathrm{s}^{-1}$ and $(2\pi)10\times10^6\ \mathrm{s}^{-1}$, corresponding to a range of intensities from $0.004\ \mathrm{W/cm}^2$ up to $40\ \mathrm{W/cm}^2$. It is clear that the peak beat frequency increases and then saturates at the highest intensities. In the experiments, the average intracavity power is on the order of 100 mW. If we consider the strongest mode of the laser to contain about 30% of the energy (see Fig. 3), and assume a spot size in the interaction region of $\sim\pi(0.15\ \mathrm{cm})^2$, then the intensity of this mode is about $400\ \mathrm{mW/cm}^2$. This is about one-fourth the intensity of the curve in Fig. 8(b) for which the Rabi frequencies are $(2\pi)2\times10^6\ \mathrm{s}^{-1}$.

Good qualitative agreement exists between the experimentally measured result in Fig. 4(c) and the calculated narrow resonances shown in Fig. 8(b). The general shapes are similar and the width of the resonance is on the order of a few megahertz in both cases. In addition, the amplitudes of the measured and predicted beat frequencies are of the same order of magnitude. The much broader features of Fig. 8(a) occur over a range of magnetic fields which could not be covered with the Helmholtz coils used to scan the magnetic field in Fig. 4. An interesting feature of Fig. 8 is that the slope of the beat frequency within a few Gauss of the zero is opposite the slope of the general trend of the signal which occurs over a range of ±50 G. In addition, a rough comparison of these slopes indicates that the magnetic field dependence of the nonlinear response is approximately 500 times greater than the linear response. As seen in the inset of Fig. 8(a), the magnitude of the slope of the beat frequency about zero magnetic field is 200 kHz/G. If the Doppler width could be decreased to a few MHz, this slope would increase by a factor of 50. Increasing the number density and decreasing the intensity (to the point of less saturation) would both act to further increase the slope. In principle, this sensitivity could be exploited to make measurements of small magnetic fields, or as an error signal for stabilization of the laser cavity.

With the coarse techniques employed in tuning the laser to resonance with the 653.86 nm transition, it is unlikely that the laser frequency be set at the center of the Doppler-broadened line. In fact, it is more probable that the laser tends to operate in the wings of the Doppler profile. It is therefore necessary to ask what effect detuning the fields will have on the beat frequency. A reasonable first guess is that with fewer atoms to interact with, the magnitude of the beat

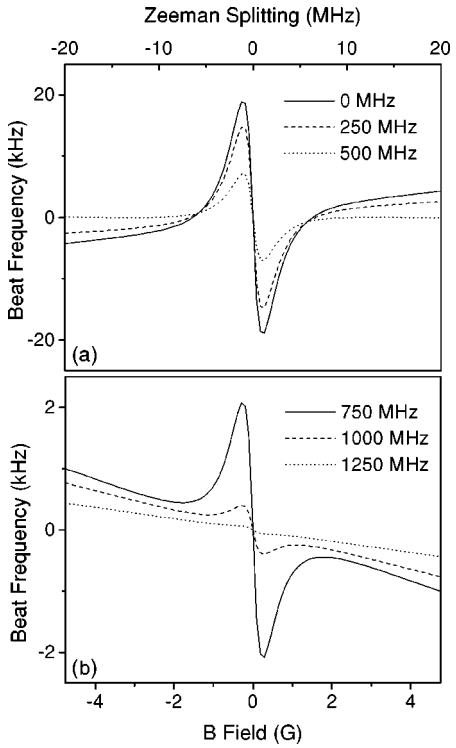

FIG. 9. Dependence of the beat frequency on the detuning $\Delta_{0+}=\Delta_{0-}$ of the two fields from the Doppler line center. Note the difference in the vertical scales for plots (a) and (b).

frequency will vary less. To account for this in the numerical simulations we define Δ_{0+} and Δ_{0-} to be additional detunings of both E_+ and E_- from the Doppler line center. The calculations shown in Fig. 9 indicate that the magnitude of the beat frequency does indeed decrease. In addition, it is seen that the shape of the beat frequency signal changes as well, becoming flatter at higher magnetic fields. Here we see that the visual agreement between these curves and the measured data improves for values of $\Delta_{0+}=\Delta_{0-}$ greater than 750 MHz. Detuning from line center also reduces the amplitude of the predicted beat frequency by about a factor of 50 in the case of $\Delta_{0+}=\Delta_{0-}=1000$ MHz.

As already mentioned, the very fact that nonlinear Faraday signals are measured at all is a consequence of coherence between the two lower Zeeman sublevels. Using the pressure-dependent dephasing rates given in Table I, we can investigate the dependence of the predicted beat frequency on the buffer gas pressure. The results are shown in Fig. 10, where the beat frequency is plotted for various values of the neon buffer gas pressure. For all curves, $\Delta_{0+}=\Delta_{0-}=500$ MHz. In this figure, it is interesting to note that the slope of the signal near zero field does not change appreciably with the increasing buffer gas pressure, although the amplitude of the signal in the same region drops almost in half. This is also the case for the 20, 50, and 100 mTorr experimental curves of Fig. 6, although at higher pressures the measured curves flatten out much more rapidly than the calculated ones.

The dark state measured in Fig. 7 is a further indication of the coherent nature of the interaction between the light fields and the samarium. The mathematical model described above also predicts the existence of this phenomenon as shown in

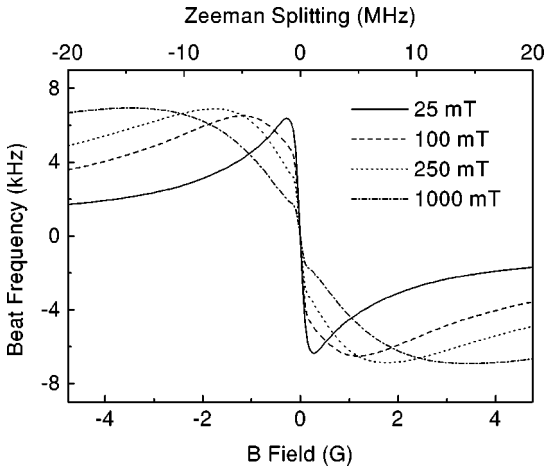

FIG. 10. Calculated beat frequency as a function of applied magnetic field for various neon buffer gas pressures.

Fig. 11. Here the system parameters were fixed at those given in Table I, with $\Delta_{0+}=\Delta_{0-}=0$. The Doppler-averaged upper-state population $\bar{\rho}_{11}$ is plotted as a function of applied magnetic field. For very large magnetic fields (not shown in Fig. 11) , the Zeeman splitting is so great that the two fields are completely out of resonance with the Doppler-broadened transition and $\bar{\rho}_{11}=0$. Then as the magnetic field is reduced the fields begin to pump more atoms into the excited state. More atoms in the excited state means more fluorescence. This trend continues until the magnetic field is zero and both fields are in resonance with the same Doppler velocity group of atoms, which are optically pumped and trapped in a coherent superposition of the $m_j=\pm 1$ sublevels. As already noted, these atoms no longer absorb the fields because destructive interference occurs between the two excitation paths. Consequently, the population of the upper level drops sharply and is accompanied by the observed drop in fluorescence.

Because the actual experiments employed time-dependent fields (two counterpropagating trains of square pulses with period of 13.4 ns), checks were made of the validity of the single-mode, steady-state approximation used in the previous numerical results. The most straightforward estimate of the

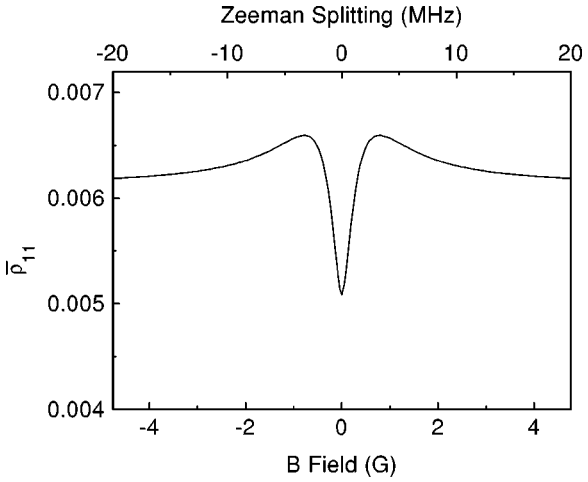

FIG. 11. The Doppler-averaged population of the upper level $(J=0)$ of the Λ system as a function of the magnetic field.

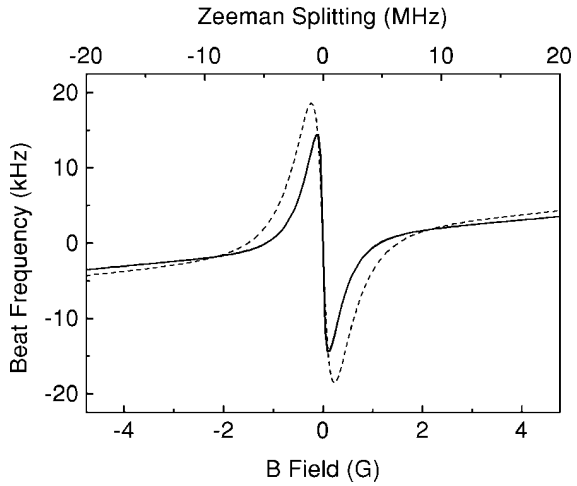

FIG. 12. The average beat frequency of five pairs of longitudinal modes corresponding to spectrum of Fig. 3. The dashed line is the calculated beat frequency assuming a single pair of longitudinal modes.

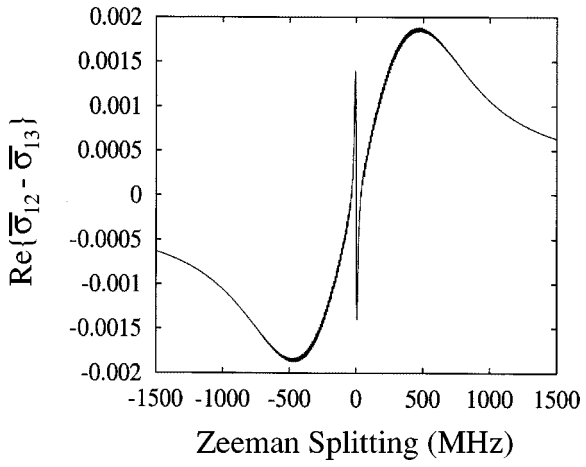

FIG. 13. Plot of the real part of $\bar{\sigma}_{12}-\bar{\sigma}_{13}$ for the situation involving two counterpropagating linearly polarized fields.

influence of the additional longitudinal modes is to treat all modes as being independent in their interactions with the samarium. This assumption is valid because the mode spacing ($\sim$75 MHz) is much greater than the natural linewidth of the transition and the response of the three-level system, as seen in the previous calculation. In addition, since only small magnetic fields are considered, the lower level splitting is always less than the cavity frequency, eliminating the resonant driving of σ_{23}. Within this approximation, the measured beat frequency is simply the average beat frequency between the different counterpropagating mode pairs. However, this average beat frequency does not differ strongly from the beat frequency between a single pair of longitudinal modes. A calculation illustrating this is presented in Fig. 12. In this calculation, Eqs. (3) were solved separately for five pairs of longitudinal modes with detunings and amplitudes given by the data of Fig. 3. The resulting beat frequencies from the five pairs of modes were then averaged to give the result which is plotted. For comparison with the calculations of Fig. 8, the strongest mode pair $[(\nu-\nu_0)/\Delta\nu_{\mathrm{FSR}}=0]$ was assumed to be at Doppler line center, and to have intensities such that $\kappa\mathcal{E}_+=\kappa\mathcal{E}_-=(2\pi)2\times10^6$ s^{-1}. In Fig. 12 the previously calculated beat frequency for a single pair of longitudinal modes with the same Rabi frequency is also plotted as the dashed line. As an additional check, the time-dependent differential equations of Eqs. (3) were integrated numerically assuming excitation by two pulse trains of square pulses. The results of these calculations show that after some initial oscillation, all the density matrix elements relax to constant values on the time scale of 5–10 μs. Furthermore, the calculated final values of the density matrix elements (with time-dependent fields) are nearly identical to those obtained by solving Eqs. (3) in steady state with constant fields. From a physical standpoint, this is to be expected since the characteristic relaxation rates of the atomic system all occur on a time scale which is much slower than the round-trip time of the laser cavity.

The reasonably good agreement between the experiment and the calculations leads us to conclude that the single-mode, steady-state model, which was initially presented, adequately describes the major features of the measurements. The theory confirms the approximate spectral width of the measured signals, the dependence on buffer gas pressure, and the existence of the dark state. In addition, the theoretical results suggest that saturation and detuning from the Doppler line center both contribute to the observed signals. The major shortcoming of the theory is its failure to accurately predict the shape of the beat frequency signal in the wings. Except in the cases of high intensity and large detuning from Doppler line center, the calculated signals always returned to near zero faster than the measured signals. Probable causes for this behavior are spatial inhomogeneities of the magnetic field, frequency instability of the laser, and the influence of the odd isotopes—all of which act as broadening mechanisms.

VI. CONCLUSION

In summary, a technique of differential intracavity phase spectroscopy has been presented, and encouraging proof-of-principle experiments have been performed with samarium vapor inside a unique ring laser with a linear tail. In its current implementation, the technique permits the direct measurement of phase shifts between the counterpropagating fields with an accuracy close to 10^{-6}. The greatest benefit of this technique lies in its potential sensitivity, which will only be attained when the frequency stability and control of the laser has been improved. The most straightforward means of accomplishing this is to lock the laser frequency to the Doppler absorption peak of one of the even samarium isotopes in an external vapor cell. Locking to the samarium transition in an external cell would present several advantages and possibilities. It would improve the frequency stability of the laser, and ensure that the laser is tuned to a known point of the samarium spectrum. In addition, with the laser locked to the center of the Doppler profile data could be acquired at slower rates, enabling one to take full advantage of signal averaging. Furthermore, the linear part of the laser could then be removed, permitting Doppler-free experiments in the ring cavity itself, using a small vapor cell or atomic beam mounted

between quarter-wave plates. In this situation, one could envision using the narrow resonance of the beat frequency (as seen in Fig. 4) as the actual error signal for locking the laser to the center of the Doppler-broadened transition. Here it would be possible to use the laser as a sensitive magnetometer, with the error signal being proportional to small applied magnetic fields. A different approach, which could eliminate some of the uncertainties with the bias, would be to use a linear cavity with two pulses per cavity round-trip time [35]. This might be the appropriate choice when attempting to stabilize the difference frequency between the two pulse trains to the splitting of two hyperfine levels. In any case, stabilization to a high finesse Fabry-Pérot cavity [36] could reduce the uncertainty in the beat frequency to the millihertz range, which implies a phase sensitivity of 10^{-12} radians. Finally, accurate stabilization of the cavity to a known optical transition would present a unique possibility for using the multimode laser as a frequency reference in three different frequency regimes: the optical, the rf (given by the longitudinal mode spacing), and the audio range (given by the beat frequency between the counterpropagating fields).

ACKNOWLEDGMENTS

This work was supported by the National Science Foundation under Grant No. ECS-9219450. S. D. was supported, in part, by the Center for Advanced Studies of the University of New Mexico.

APPENDIX: ANALYSIS WITH LINEARLY POLARIZED COUNTERPROPAGATING FIELDS

We have analyzed another more complex situation than that which we presented above. The following situation involves two linearly polarized counterpropagating fields in a ring laser interacting with an intracavity vapor of samarium atoms. The three-level system is the same as described previously, but this situation is more complicated because each field in the system of density matrix equations has to be replaced by a sum of two fields with opposite wave vector. The two density matrix elements ρ_{12} and ρ_{13} have two components corresponding to the $+k$ and $-k$ wave vectors. The three diagonal elements ρ_{11}, ρ_{22}, and ρ_{33} and the off-diagonal element ρ_{23} each have three components: One component with no spatial dependence and two components with wave vectors $+2k$ and $-2k$ responsible for a standing wave pattern. In all, there are 16 coupled (complex-valued) equations describing the system.

An example solution of this system is shown in Fig. 13. In this figure we plot the real part of the difference of the two matrix elements responsible for the beat frequency ($\overline{\sigma}_{12} - \overline{\sigma}_{13}$), as a function of detuning (splitting) of the two lower levels. Parameters used are those of Table I. As seen, this system yields qualitatively the same results as the system considered in the main text.

[1] W. Demtröder, *Laser Spectroscopy*, 2nd ed. (Springer-Verlag, Berlin, 1996).
[2] P. E. Toschek and V. M. Baev, in *Lasers, Spectroscopy and New Ideas: A Tribute to Arthur L. Schawlow*, edited by W. M. Yen and M. D. Levenson (Springer-Verlag, Berlin, 1987), pp. 89–111.
[3] F. Aronowitz and R. J. Collins, Appl. Phys. Lett. **9**, 55 (1966).
[4] F. Aronowitz and R. J. Collins, J. Appl. Phys. **41**, 130 (1970).
[5] S. Diddams, B. Atherton, and J.-C. Diels, Opt. Commun. **143**, 252 (1997).
[6] M. L. Dennis, J.-C. M. Diels, and M. Lai, Opt. Lett. **16**, 529 (1991).
[7] M. Lai, J.-C. Diels, and M. L. Dennis, Opt. Lett. **17**, 1535 (1992).
[8] S. Diddams, B. Atherton, and J.-C. Diels, Appl. Phys. B: Lasers Opt. **63**, 473 (1996).
[9] W. C. Martin, R. Zalubas, and L. Hagan, *Atomic Energy Levels: The Rare-Earth Elements* (U. S. Department of Commerce, National Bureau of Standards, Washington, DC, 1978).
[10] J. Mlynek and W. Lange, Opt. Commun. **30**, 337 (1979).
[11] C. Parigger, P. Hannaford, and W. J. Sandle, Phys. Rev. A **34**, 2058 (1986).
[12] I. O. G. Davies, P. E. G. Baird, and J. L. Nicol, J. Phys. B **20**, 5371 (1987).
[13] K. H. Drake, W. Lange, and J. Mlynek, Opt. Commun. **66**, 315 (1988).
[14] L. M. Barkov, D. A. Melik-Pashayev, and M. S. Zolotorev, Opt. Commun. **70**, 467 (1989).
[15] P. E. G. Baird, M. Irie, and T. D. Wolfenden, J. Phys. B **22**, 1733 (1989).
[16] R. J. McLean, P. Hannaford, and R. M. Lowe, Phys. Rev. A **42**, 6616 (1990).
[17] W. Gawlik, J. Kowalski, R. Neumann, and F. Träger, Opt. Commun. **12**, 400 (1977).
[18] S. Giraud-Cotton, V. P. Kaftandjian, and L. Klein, Phys. Lett. **88A**, 453 (1985).
[19] W. Gawlik and J. Zachorowski, J. Phys. B **20**, 5939 (1987).
[20] J. Ye, L.-S. Ma, and J. L. Hall, Opt. Lett. **21**, 1000 (1996).
[21] J. Ye, L.-S. Ma, and J. L. Hall, J. Opt. Soc. Am. B **15**, 6 (1998).
[22] P. E. G. Baird *et al.*, Phys. Rev. Lett. **39**, 798 (1977).
[23] M. J. D. Macpherson *et al.*, Phys. Rev. Lett. **67**, 2784 (1991).
[24] N. H. Edwards, S. J. Phipp, P. E. G. Baird, and S. Nakayama, Phys. Rev. Lett. **74**, 2654 (1995).
[25] P. Lett and L. Mandel, J. Opt. Soc. Am. B **2**, 1615 (1985).
[26] A. N. Nesmeianov, *Vapor Pressure of the Chemical Elements* (Elsevier, Amsterdam, 1963).
[27] S. A. Diddams, Ph.D. thesis, University of New Mexico, 1996.
[28] H. Brand, B. Nottbeck, H. H. Schulz, and A. Stuedel, J. Phys. B **11**, L99 (1978).
[29] A. Siegman, *Lasers* (University Science Books, Mill Valley, CA, 1986).
[30] G. Alzetta, A. Gozzini, L. Moi, and G. Orriols, Nuovo Cimento B **52**, 209 (1979).
[31] E. Arimondo and G. Orriols, Lett. Nuovo Cimento **17**, 333 (1976).

[32] G. Alzetta, L. Moi, and G. Orriols, Nuovo Cimento B **52**, 209 (1979).
[33] G. Orriols, Nuovo Cimento B **53**, 1 (1979).
[34] R. M. Lowe, D. S. Gough, R. J. McLean, and P. Hannaford, Phys. Rev. A **36**, 5490 (1987).
[35] M. J. Bohn and J.-C. Diels, Opt. Lett. **22**, 642 (1997).
[36] R. W. P. Drever *et al.*, Appl. Phys. B: Photophys. Laser Chem. **31**, 97 (1983).